Antarctic Science 30(5), 307–321 (2018) © Antarctic Science Ltd 2018 doi:10.1017/S0954102018000299

Suspected meteorite fragments in marine sediments from East Antarctica

NARESH C. PANT[1], FRANCISCO J. JIMENEZ-ESPEJO[2], CARY P. COOK[3,4], PAROMITA BISWAS[1], ROBERT MCKAY[5], CLAUDIO MARCHESI[6,7], MOTOO ITO[8], DEWASHISH UPADHYAY[9], JUNICHIRO KURODA[2], KENJI SHIMIZU[8], RYOKO SENDA[10], TINA VAN DE FLIERDT[11], YOSHINORI TAKANO[2], KATSUHIKO SUZUKI[2], CARLOTA ESCUTIA[7] and PRAKASH K. SHRIVASTAVA[12]

[1]*Centre for Advanced Studies, Department of Geology, University of Delhi, Delhi-11007, India*
[2]*Japan Agency for Marine-Earth Science and Technology, Yokosuka 237-0061, Japan*
[3]*The Grantham Institute for Climate Change, Imperial College London, London SW7 2AZ, UK*
[4]*Department of Geological Sciences, University of Florida, Gainesville, FL 32611, USA*
[5]*Antarctic Research Centre, Victoria University of Wellington, PO Box 600, Wellington 6140, New Zealand*
[6]*Departamento de Mineralogía y Petrología, UGR, 18002 Granada, Spain*
[7]*Instituto Andaluz de Ciencias de la Tierra, CSIC-UGR, 18100 Armilla, Granada, Spain*
[8]*Kochi Institute for Core Sample Research, JAMSTEC, Kochi 783-8502, Japan*
[9]*Department of Geology and Geophysics, Indian Institute of Technology, Kharagpur, 721302 Kharagpur, India*
[10]*Faculty of Social and Cultural Studies, Kyushu University, 744, Motooka Nishi-ku Fukuoka, 819-0395, Japan*
[11]*Department of Earth Science and Engineering, Imperial College London, London SW7 2AZ, UK*
[12]*Geological Survey of India, Faridabad, India*
fjjspejo@jamstec.go.jp

Abstract: Unusual mafic rock fragments deposited in Plio-Pleistocene-aged marine sediments were recorded at Integrated Ocean Drilling Program (IODP) Site U1359, in Wilkes Land, East Antarctica. These fragments were identified from sediment layers deposited between *c.* 3 and 1.2 Ma, indicating a sustained supply during this time interval. Clinopyroxenes in these basalts are Al–Ti diopside–hedenbergite, uncommon in terrestrial magmatic rocks. A single strong peak in the Raman spectra of a phosphate-bearing mineral at 963 cm^{-1} supports the presence of merrillite. Although not conclusive, petrological traits and oxygen isotopic compositions also suggest that the fragments may be extra-terrestrial fragments affected by shock metamorphism. Nevertheless, it is concluded that the basaltic fragments incorporated in marine sediments at Site U1359 represent ice-rafted material supplied to the continental rise of East Antarctica, probably from the bedrocks near the proximal Ninnis Glacier. Further studies on Plio-Pleistocene sediments near Site U1359 are required to characterize the unusual mafic rocks described.

Received 29 December 2017, accepted 20 June 2018

Key words: Adélie Coast, achondrite-type meteorite, ice-rafting, oxygen isotopes

Introduction

Meteorites in glaciers have been reported in both Hemispheres (e.g. Floss *et al.* 2003, Keil 2012). Besides, large extra-terrestrial dust horizons in East Antarctica are also known (e.g. Misawa *et al.* 2010). Ice-rafted debris (IRD) may therefore be a potential material to search for meteorites in Antarctica.

During the study of Plio-Pleistocene sediments recovered during Integrated Ocean Drilling Program (IODP) Expedition 318 off the coast of Terre Adélie in East Antarctica (IODP Site U1359) (Fig. 1) (Escutia *et al.* 2011), four small rock fragments (*c.* 100–200 μm) with typical igneous texture were recovered. The examined sediment sequence represents a time interval spread over *c.* 2 million years. In this study, detailed mineralogical and geochemical characterization is presented to suggest the possible extra-terrestrial nature of these rock fragments. Identification of the terrestrial or extra-terrestrial nature of grains has significance for the provenance, depositional model of sediments, and geology of the ice-covered Antarctic continent.

Materials

IODP Site U1359 (64°54'S, 143°57'E) was drilled at 4003 m of water depth on the eastern levee of the Jussieu submarine channel, *c.* 270 km from the Terre Adélie margin (East Antarctica) (Figs 1 & 2) (Escutia *et al.* 2011). Four adjacent cores were collected at Site U1359, from which a composite 'spliced' complete record of the upper 200 m was obtained, with depths reported here in metres composite depth (mcd). Sediments in this interval are mainly composed of interbedded pelagic diatom-rich muds and terrigenous clays and silts (Fig. 3)

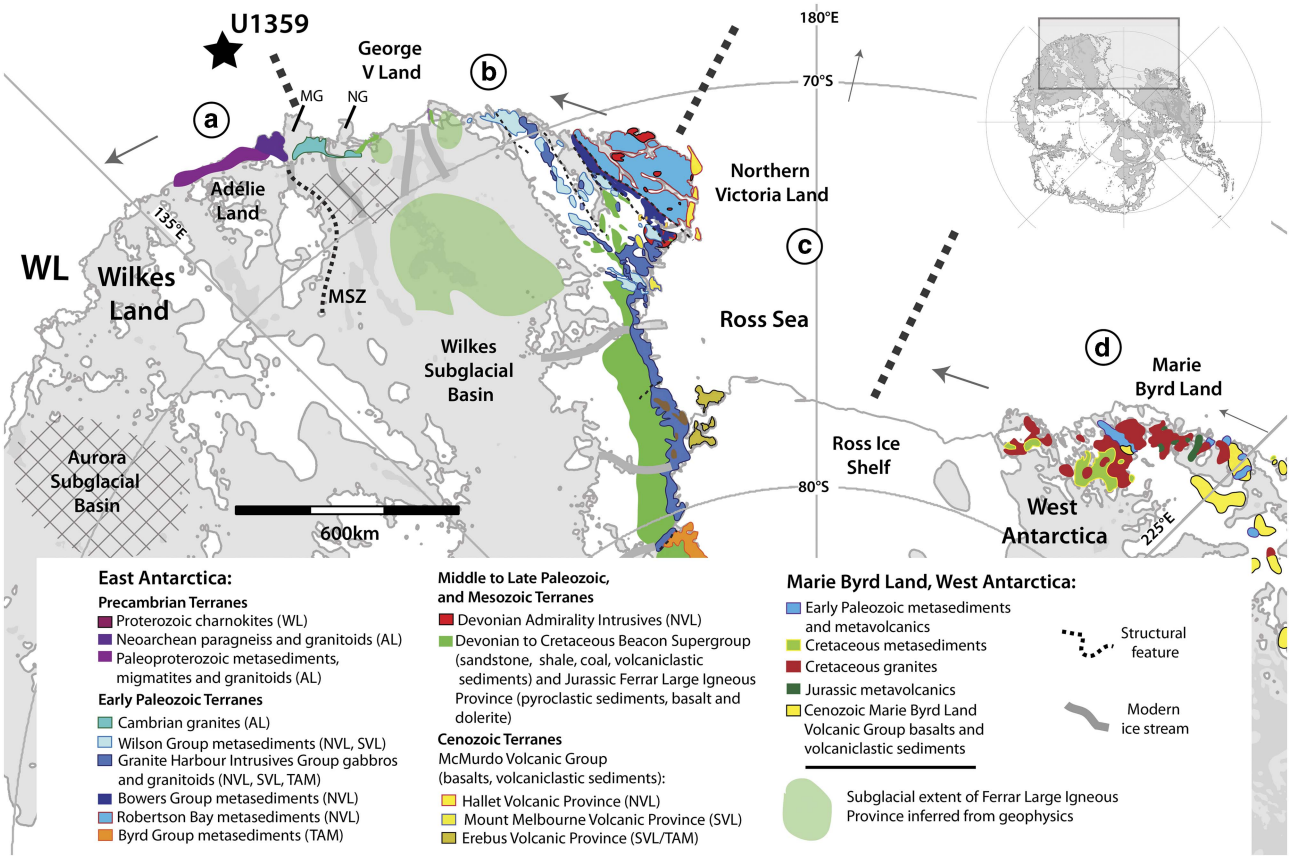

Fig. 1. Geological map of East Antarctica and Marie Byrd Land, modified from Goodge & Fanning (2010). The figure shows the outcrops of known bedrock terranes and inferred subglacial geology. The base map is from BEDMAP-2, with grey areas below sea level (Fretwell *et al.* 2013), modified using ARCGIS software. Four different provenance sectors, delimited by dashed bold lines, could supply IRD to the studied sediments: **a.** Terre Adélie, **b.** George V Land and the Wilkes Subglacial Basin, **c.** Ross Sea, and **d.** West Antarctica. Arrows offshore show the direction of iceberg-transport in a counter-clockwise direction. NG: Ninnis Glacier Tongue, MG: Mertz Glacier Tongue, MSZ: Mertz Shear Zone.

(Tauxe *et al.* 2012, Patterson *et al.* 2014). Natural gamma radiation (NGR) shows cyclic variations and points to a well-preserved palaeoenvironmental record forced by millennial orbital oscillations, as described in nearby sites (Patterson *et al.* 2014). Magneto-biostratigraphy indicates that the oldest sediments in this section are *c.* 6.5 Ma in age (Escutia *et al.* 2011, Tauxe *et al.* 2012). Currently, sediments are supplied to the Terre Adélie margin by hemipelagic deposition, downslope processes, ocean currents and ice-rafting.

Initial studies on sediments from Site U1359 aimed to characterize the contents and composition of ice-rafted heavy minerals. For this purpose, sampling was carried out at *c.* 1 m intervals throughout the upper 200 m of the cores. However, in this study, given the low quantities of minerals recovered in individual intervals, samples were combined to obtain statistically robust amounts of material. A total of 32 combined samples were created, each one representing *c.* 3–8 m bins. During subsequent analysis, basaltic fragments (F) were collected from four of these binned sedimentary intervals. Fragment F1 was recovered from a sample representing 31.13–25.75 mcd, F2 at 36.63–33.63 mcd, F3 at 50.13–46.21 mcd, and F4 at 55.44–51.13 mcd (Table I). These four basaltic fragments with high Al–Ti diopside–hedenbergite were not found elsewhere in the core section (Fig. 3). The interval corresponding to the deepest recovered fragment was deposited at *c.* 2.7 Ma (Middle Pliocene), and the two shallowest intervals were deposited between *c.* 2.15 and *c.* 1.01 Ma (Plio-Pleistocene), with one depositional hiatus of *c.* 0.6 Ma (Tauxe *et al.* 2012).

Methods

Heavy mineral separation and major element analyses

Detrital fractions >150 μm were subjected to mineral separation using bromoform heavy liquid. The heavy

https://doi.org/10.1017/S0954102018000299 Published online by Cambridge University Press

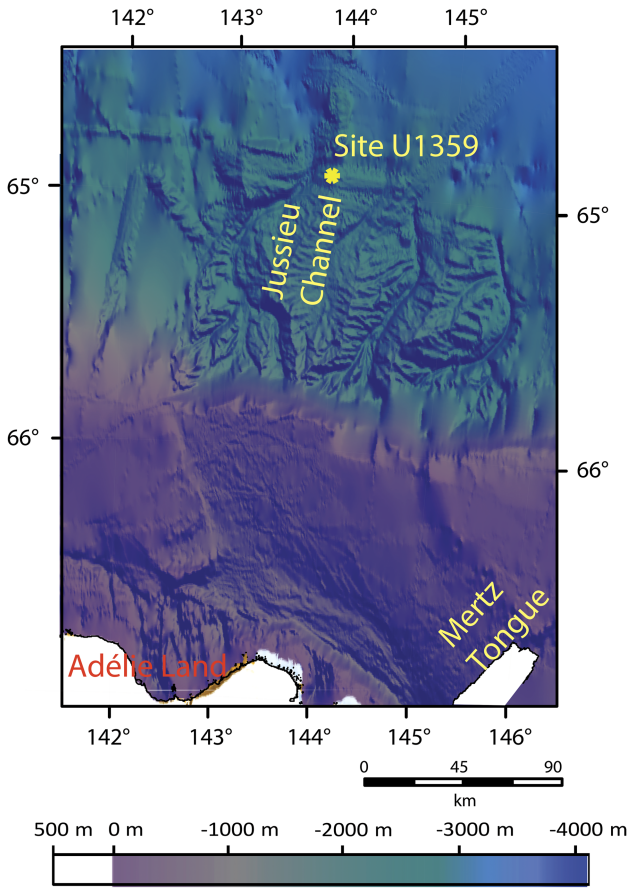

Fig. 2. Bathymetric map of the Adélie Coast continental margin, showing the topography of the shelf, slope and rise, the main canyons crossing the area, and the location of IODP Site U1359.

mineral fractions were then mounted on a glass slide with cold-fixing epoxy (araldite), polished and analysed using a scanning electron microscope (SEM) and electron probe microanalyser (EPMA). The SEM analyses were carried out at the Department of Geology, University of Delhi (India), using a Zeiss SEM equipped with a Cambridge energy dispersive spectrometer (EDS). The EPMA analyses were performed at the Geological Survey of India, Faridabad, using a CAMECA SX100 EPMA equipped with four spectrometers. The operating conditions were 15 kV accelerating voltage, 10 nA beam current and 1 μm beam diameter. Major element compositions of minerals and glass are presented in Tables II, III and IV.

LA–ICP–MS analyses of clinopyroxene

Trace element abundances of clinopyroxene within basaltic fragment F2 (Table V) were analysed by laser ablation–inductively coupled plasma–mass spectrometry (LA–ICP–MS) at the Department of Geology and Geophysics, Indian Institute of Technology, Kharagpur, using a Cetac 213 nm Nd YAG laser ablation system connected to a Varian 820 (now Bruker) quadrupole ICP–MS. Sites were ablated in thin sections at 5 Hz pulse frequency, 12 μm spot size, and 730 V energy. Analyses were done in peak hopping mode and each analysis consisted of 20 s background measurement and 40 s peak signal measurement. Calibration was done using the National Institute of Standards and Technology 610 glass, and data were treated using the Glitter© software, considering ^{44}Ca from EPMA analyses as the internal standard. Typical uncertainties are in the range of 5–15% (1σ) for most elements.

Oxygen isotope analyses

Oxygen isotopic measurements were performed on clinopyroxene grains by *in situ* analysis using the JAMSTEC NanoSIMS 50L at Kochi Institute for Core Sample Research following the technique described by Ito and Messenger (2008). A focused primary Cs^+ beam of *c.* 2.5 pA was rastered over 8 × 8 or 10 × 10 μm areas on the fragment F4, with San Carlos olivine as an analytical standard. Negative secondary ions of ^{16}O, ^{17}O, ^{18}O, ^{28}Si, $^{26}Mg^{16}O$ and $^{27}Al^{16}O$ were measured by six electron multipliers in multidetection mode at a high mass resolution of $M/\Delta M = \sim 9500$, which is sufficient to separate interfering ^{16}OH from ^{17}O. The interference was always negligible (typically < 0.1‰) in the $\delta^{17}O$ notation. A normal-incident electron gun was utilized for charge compensation of the analysis area. Each imaging run repeatedly scanned (20–30 times) the same area, with individual images consisting of 256 × 256 pixels, having a dwell time of 1000 μs per pixel. The total acquisition time ranged from 20 to 30 minutes. Each run was started after stabilization of the secondary ion beam following 5 minutes of pre-sputtering. Data were corrected for SEM dead time (44 ns) and quasi-simultaneous arrival effect using Interactive Data Language-based NASA Johnson Space Center imaging software for NanoSIMS (Ito & Messenger 2008). The measurement conditions, the instrumental mass fractionation for isotopic ratios, and the precision (*c.* 2.5‰ for $\delta^{17}O$ and *c.* 1.2‰ for $\delta^{18}O$) and accuracy for O isotopic measurement were evaluated through analyses of San Carlos olivine as a terrestrial standard. Results of oxygen isotopic analyses are in Table VI.

Raman spectroscopy

To identify mineral phases in fragment F4, a laser Raman confocal microscope (NanoPhoton RAMAN Touch) at the NanoPhoton Company (Japan) was used. Excitation was effected using the 532 nm of a Nd-YAG laser with a nominal power of 1.1 mW, and spectra were recorded by

https://doi.org/10.1017/S0954102018000299 Published online by Cambridge University Press

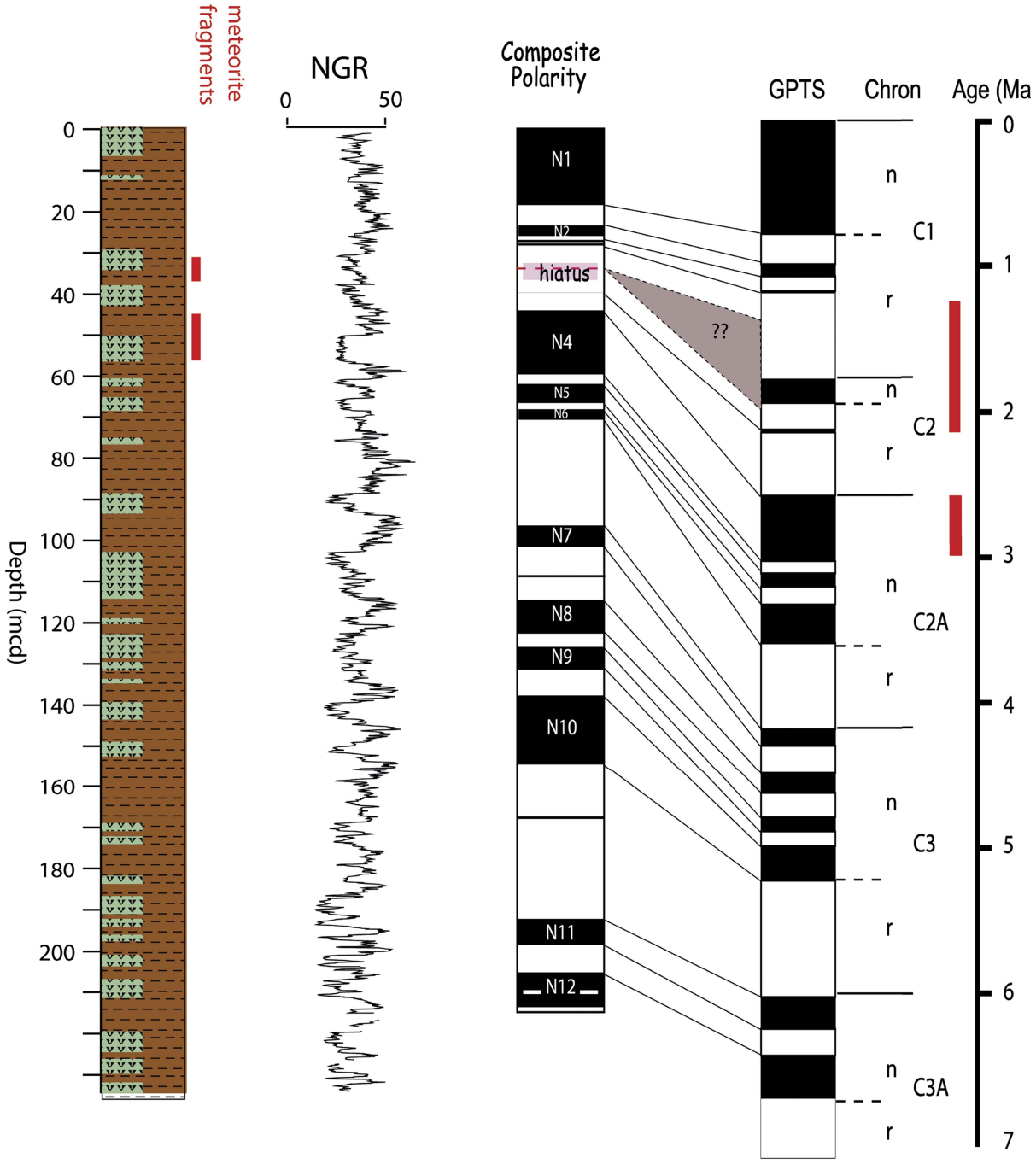

Fig. 3. Composite lithology, natural gamma radiation (NGR), polarity, geomagnetic polarity time scale (GPTS) and age plot for IODP Site U1359. Diatom rich mud is represented by green shading with chevrons, and terrigenous clays by brown shading with dashed lines. The presence of basaltic fragments is indicated by red vertical bars. Note the presence of basaltic fragments on both sides of the sedimentary hiatus.

3–30 accumulations (40 s per exposure) with a microscope objective of 100 × from an optical footprint of *c.* 0.5 μm diameter. Spectra were obtained with a 600 mm grating and 500 mm focal length spectrometer, giving a spectral resolution of *c.* 4 cm^{-1}.

Results

Four basaltic rock fragments were collected from composite heavy fractions recovered from depths of 26–56 mcd (F1–F4, Fig. 3, Table I). Fragments have sub-rounded to sub-angular shapes and sizes between

https://doi.org/10.1017/S0954102018000299 Published online by Cambridge University Press

Table I. Stratigraphic information of sediments studied at IODP site U1359.

SL.no.	Site	Hole	Core	Core type	Section	Sample interval top–bottom (cm)	Sample depth (mbsf)	Sample depth (mcd)
Sample I								
1	U1359	B	3	H	1	36–38	15.96	15.6
2	U1359	B	3	H	1	124–126	16.84	16.48
3	U1359	B	3	H	2	14–16	17.24	17.1
4	U1359	B	3	H	2	124–126	18.34	18.2
5	U1359	B	3	H	3	124–126	19.84	19.6
Sample II								
6	U1359	B	3	H	4	24–26	20.34	20.1
7	U1359	B	3	H	4	126–128	21.36	21.12
8	U1359	B	3	H	6	26–28	23.36	22.6
9	U1359	B	3	H	6	124–126	24.34	23.1
10	U1359	B	4	H	1	124–126	25.99	23.9
Sample III, Fragment F1								
11	U1359	B	4	H	2	10–12	26.35	25.75
12	U1359	C	4	H	1	22–24	29.85	26.25
13	U1359	C	4	H	1	122–124	30.85	29.63
14	U1359	C	4	H	2	122–124	32.35	30.63
15	U1359	C	4	H	3	122–124	33.85	31.13
Sample IV, Fragment F2								
16	U1359	C	4	H	4	122–124	35.35	33.63
17	U1359	C	4	H	5	122–124	36.85	34.13
18	U1359	B	5	H	1	24–26	37.06	35.13
19	U1359	C	4	H	6	122–124	38.35	36.63
Sample V								
20	U1359	C	5	H	1	22–24	39.35	36.82
21	U1359	C	5	H	1	122–124	40.35	37.13
22	U1359	B	5	H	4	24–26	41.56	39.13
23	U1359	C	5	H	3	22–24	42.35	40.13
24	U1359	C	5	H	4	122–124	44.85	41.32
Sample VI								
25	U1359	C	5	H	4	122–124	44.85	42.13
26	U1359	C	5	H	5	22–24	45.35	43.13
27	U1359	B	6	H	2	24–26	45.45	44.63
28	U1359	B	6	H	2	124–126	46.45	45.13
29	U1359	C	5	H	6	122–124	47.85	45.21
Sample VII, Fragment F3								
30	U1359	B	6	H	4	24–26	48.45	46.21
31	U1359	B	6	H	4	124–126	49.45	47.63
32	U1359	C	6	H	2	22–24	50.35	48.21
33	U1359	C	6	H	2	122–124	51.35	49.21
34	U1359	C	6	H	3	122–124	52.85	50.13
Sample VIII, Fragment F4								
35	U1359	C	6	H	4	22–24	53.35	51.13
36	U1359	C	6	H	4	122–124	54.35	52.63
37	U1359	B	7	H	2	24–26	55.68	53.13
38	U1359	C	6	H	6	22–24	56.35	54.13
39	U1359	C	6	H	6	119–121	57.32	55.44

c. 150 μm and 400 μm. All fragments were analysed by electron microscopy. Because of reduced sample amounts, different types of analyses were performed in each fragment. The most representative results are presented here. Major element composition of clinopyroxenes was measured at fragments F2, F3 and F4. Sample F2 was selected for rare earth element (REE) analysis of clinopyroxenes and major element measurements in plagioclase and glass; sample F3 for analyses of major elements in titaniferous magnetite, ilmenite and merrillite, as well as Raman spectroscopy; and sample F4 for oxygen isotope analysis.

Petrography of basalt fragments and major and trace element compositions of minerals and glass

Optical microscopy of basaltic grains was not possible because of the small size and the nature of grain mounts. The petrological description is therefore based on

https://doi.org/10.1017/S0954102018000299 Published online by Cambridge University Press

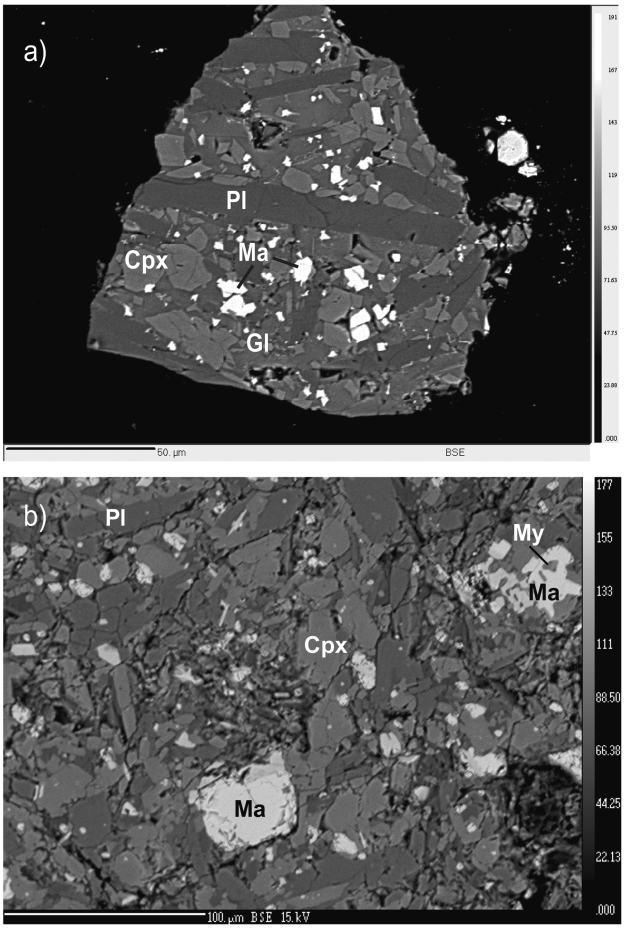

Fig. 4. a. Back-scattered electron (BSE) image of basaltic fragment F3 from Site U1359. Note euhedral to subhedral laths of plagioclase (Pl) of variable size, glass (Gl) in the matrix (spotted), and subhedral clinopyroxene (Cpx). Plagioclase and clinopyroxene appear unzoned in the BSE image. **b.** BSE image of basaltic fragment from Site U1359. Note inclusion of a merrillite grain (My) in magnetite (Ma).

scanning electron microscopy. The fragments have intergranular texture, and backscattered electron (BSE) imaging for fragments F2 and F3 revealed four distinct grey tone areas (Fig. 4). The darkest tone corresponds to subhedral–euhedral laths (up to 120 µm long) of plagioclase, constituting *c.* 40% of the rock (Fig. 4). The major mafic phase consists of prismatic to stocky, subhedral grains of clinopyroxene (light grey) up to 30 µm in diameter, constituting 25–30% of the rock. In addition, the rock fragments contain a significant amount of glass/melt fraction (*c.* 20%), with the glass having a diffused and spotted appearance and a variable composition (Table II), represented by a grey tone intermediate between that of plagioclase and clinopyroxene (Fig. 4a). Analysis indicates the range of glass composition, from high silica to relatively low silica (Table II). Opaque phases (oxides, mainly ilmenite and titaniferous magnetite) constitute the remaining 10–15% of the mineral assemblage. In one fragment, a merrillite grain is included in magnetite (Fig. 4b).

Plagioclase components within the basalt grains are generally calcium-rich ($An_{55\text{-}72}$) but show a significant compositional variation, with some grains having high Na content (up to Ab_{65}, Table II).

Clinopyroxene compositions are variable, but generally have high Al^{IV} (0.15–0.46 atoms per formula unit (a.p.f.u. on 6 oxygen basis)) and low Na (0.03–0.08 a.p.f.u) (Table III).The Ca content varies from 0.83 to 0.91 a.p.f.u., and the Ti content from 0.05 to 0.15 a.p.f.u. These high Al^{IV}, Ti and Ca concentrations imply pyroxene compositions close to the high Al–Ti diopside–hedenbergite end member (Fig. 5). Similar clinopyroxene compositions are common in angrites, a relatively rare achondrite meteorite. Fields of high Al–Ti diopside–hedenbergite from several angrites are also plotted in this figure. High Ca–Al–Ti clinopyroxene is also reported from the McMurdo Volcanic Group (MVG), but the MVG clinopyroxenes have lower Ti and Ca, and the compositional distinction is evident in Fig. 5. The concentrations of Fe^{2+} (0.11–0.31 a.p.f.u.), Mn (< 0.01 a.p.f.u.) (Fig. 6a) and Fe^{3+} (0.04–0.17 a.p.f.u.) (Table III) are generally low, whereas Ti (0.05–0.15 a.p.f.u.) is relatively high (Fig. 6b), values chondrite normalized. REE patterns of two analyses show that the clinopyroxene are fractionated ($La_N/Yb_N = 0.03–0.29$) and display prominent negative europium anomalies (Eu/Eu* = 0.35–0.78) (Fig. 7). These REE profiles are convex upward with depletion of light rare earth elements (LREE) ($La_N = 0.48–5.55$) and relative enrichment of heavy rare earth elements (HREE) ($Yb_N = 18–19$). For comparison, trace and REE analyses of terrestrial (green curves in Fig. 7, Northern Victoria Land) and extra-terrestrial pyroxene (clinopyroxenes of angrites represented by grey curves in Fig. 7, and Mare basalt shown as red curves) are also plotted in this figure and listed in Table V. The REE data of clinopyroxene from U1359 are represented by bold black lines in Fig. 7. The extra-terrestrial and terrestrial clinopyroxenes are distinguished by more depleted LREE, presence of europium anomaly and enriched HREE in the former. Plots of clinopyroxenes of U1359 show affinity to the extra-terrestrial patterns (Fig. 7).

Feldspars and matrix glass have highly variable compositions (SiO_2 *c.* 47–60 wt.%, Al_2O_3 *c.* 17–22 wt.%, $Na_2O + K_2O$ *c.* 8–11 wt.% and CaO *c.* 2–8 wt.%, Table II). The FeO and MgO concentrations are up to *c.* 11 wt.% and 3 wt.%, respectively.

The opaque minerals are mostly magnesian ilmenite and Mg- and Al-bearing titaniferous magnetite (Table IV). A phosphate mineral identified as merrillite is present as an inclusion in magnetite. Although the

https://doi.org/10.1017/S0954102018000299 Published online by Cambridge University Press

Table II. Major element analyses of plagioclase and glass in basaltic fragment F2 (Sample IV) from IODP site U1359.

Phase	Plagioclase						Feldspar glass		Glass	
Analysis no.	46/1	42/1	3/1	78/1	79/1	80/1	6/1	9/1	25/1	44/1
SiO_2 (wt%)	53.92	49.29	52.91	55.00	61.46	54.60	59.83	57.71	50.17	47.10
TiO_2	0.33	0.12	0.25	0.32	0.20	0.36	0.20	0.21	2.41	2.81
Al_2O_3	28.24	31.10	29.53	27.97	24.33	24.77	21.87	22.39	17.47	16.94
Cr_2O_3	0.01	0.01	0.77	0.02	0.00	0.18	1.58	1.66	0.03	0.03
BaO	0.00	0.00	0.12	0.06	0.22	0.11	0.38	0.27	0.11	0.08
FeO	0.66	0.69	0.62	1.35	0.82	1.55	0.34	0.65	11.38	10.46
MnO	0.02	0.00	0.02	0.01	0.03	0.03	0.02	0.03	0.28	0.24
MgO	0.00	0.14	0.03	0.02	0.26	1.23	0.08	0.98	2.17	2.96
CaO	12.06	15.19	11.98	11.40	6.68	11.24	2.36	4.84	4.84	8.08
Na_2O	4.81	3.09	4.47	4.81	7.81	4.89	7.04	6.65	5.10	5.87
K_2O	0.21	0.21	0.19	0.38	0.89	0.35	3.85	1.68	5.82	3.26
Total	100.32	99.85	100.89	101.45	102.90	99.51	97.55	97.07	101.19	99.56
Si	2.44	2.27	2.39	2.47	2.69	2.51				
Ti	0.01	0.00	0.01	0.01	0.01	0.01				
Al	1.51	1.69	1.57	1.48	1.26	1.34				
Cr	0.00	0.00	0.03	0.00	0.00	0.01				
Ba	0.00	0.00	0.00	0.00	0.00	0.00				
Fe^{2+}	0.02	0.03	0.02	0.05	0.03	0.06				
Mn	0.00	0.00	0.00	0.00	0.00	0.00				
Mg	0.00	0.01	0.00	0.00	0.02	0.08				
Ca	0.59	0.75	0.58	0.55	0.31	0.55				
Na	0.42	0.28	0.39	0.42	0.66	0.44				
K	0.01	0.01	0.01	0.02	0.05	0.02				
Total	5.01	5.03	5.00	5.00	5.03	5.03				
Anorthite	0.58	0.72	0.59	0.56	0.31	0.55				
Albite	0.41	0.27	0.40	0.42	0.64	0.43				
Orthoclase	0.01	0.01	0.01	0.02	0.05	0.02				

Cations calculated based on 8 oxygens

merrillite grain is >5 μm and the beam diameter for analysis was kept at 1 μm, there is a possibility of error due to matrix effect because of the volume of interaction of the beam generally being significantly larger than the beam size. The idealized formula of merrillite is $Ca_9NaMg(PO_4)_7$ and it is a common phosphate mineral in meteorites. The fluorine content of analysed merrillite is high (5.17 a.p.f.u. on 56 oxygen basis, Table IV). The Si abundance (3.43 a.p.f.u.) is also high, supporting solid solution involving PO_4-SiO_4. The Na content (1.09 a.p.f.u) is typical of merrillite composition (see discussion).

Oxygen isotopic compositions (F4) and Raman spectroscopy (F3)

A total of six oxygen three-isotope analyses were performed in four different clinopyroxene grains in the fragment F4. Compared to SMOW (Standard Mean Ocean Water), $\delta^{17}O$ ranges from 0 to 9‰ and $\delta^{18}O$ from -4 to 11‰ (Table VI). Analysis numbers of 1a, 1b and 1c are all measurements of the same clinopyroxene grain from the fragment F4. Other analyses (2–4) are different clinopyroxene grains in the fragment F4. These values of $\delta^{17}O$ and $\delta^{18}O$ are similar within analytical error to those of bulk Earth, Moon, Mars, ordinary chondrites and differentiated meteorite (e.g. howardite–eucrite–diogenite, HED) groups, and plot nearly parallel to the terrestrial fractionation line (Fig. 8). The U1359 fragment is much more homogeneous in terms of oxygen isotopes than Ca–Al-rich inclusions (CAI) in chondrites (Fig. 8).

In the fragment F3 a single strong peak at 963 cm^{-1} (error margin of ± 1 cm^{-1}) was observed in the grain, provisionally identified as a phosphate having composition similar to merrillite (Fig. 9). The Raman spectra corroborate identification as merrillite, as whitlockite has a strong laser Raman peak at 967 cm^{-1}, which is not present in the examined grain.

Discussion

Evidence for a meteorite or unprecedented mantelic origin of basalt fragments

In terrestrial mafic rocks, Al–Ti diopside–hedenbergite pyroxene, similar to grains in U1359 fragments (Fig. 5), is

https://doi.org/10.1017/S0954102018000299 Published online by Cambridge University Press

Table III. Major element analyses of clinopyroxene in basaltic fragments chondrite normalized (normalizing values from Sun & McDonough 1989).

Fragment	F2																		
Sample	IV											VII							VIII
Analysis no.	2/1	8/1	81/1	24/1	43/1	52/1	17/1	22/1	23/1	47/1	43/1	42/1	63/1	65/1	67/1	68/1	25/1	77/1	78/1
SiO_2 (wt%)	44.88	45.43	46.49	47.24	43.56	46.58	47.87	44.36	41.74	44.21	43.56	49.78	47.74	49.59	42.35	47.48	44.86	44.03	48.60
TiO_2	3.92	3.73	2.60	2.96	4.17	2.71	2.86	4.29	3.78	3.68	4.17	2.06	1.91	1.99	5.13	2.34	3.27	3.62	2.30
Al_2O_3	7.98	6.25	7.73	5.93	8.22	5.11	5.21	8.09	7.89	6.66	8.22	4.53	7.23	3.44	10.16	6.48	8.59	8.96	4.47
Cr_2O_3	0.23	0.68	0.25	0.04	0.03	0.15	0.02	0.01	7.04	0.00	0.03	0.21	0.26	0.13	0.01	0.04	0.06	0.85	0.11
BaO	0.06	0.08	0.00	0.02	0.00	0.00	0.06	0.04	0.00	0.02	0.00	0.14	0.00	0.00	0.07	0.00	0.00	0.14	0.01
FeO	8.48	9.53	6.17	7.94	9.04	8.13	8.47	8.85	8.76	9.00	9.04	10.70	6.42	10.39	8.52	7.79	7.35	6.22	7.19
MnO	0.15	0.14	0.12	0.17	0.19	0.12	0.14	0.17	0.23	0.18	0.19	0.23	0.11	0.19	0.13	0.11	0.18	0.06	0.11
MgO	11.39	10.75	12.96	12.21	10.58	13.04	12.24	10.99	9.91	11.75	10.58	12.58	13.06	12.81	9.43	12.47	11.48	12.00	13.53
CaO	22.35	21.63	22.63	22.29	21.27	22.43	21.93	22.33	20.57	22.38	21.27	20.77	21.87	20.87	22.11	21.87	22.69	22.33	22.55
Na_2O	0.53	0.52	0.48	0.55	1.05	0.52	0.51	0.62	0.59	0.53	1.05	0.43	0.52	0.50	0.67	0.52	0.55	0.48	0.43
K_2O	0.01	0.00	0.05	0.00	0.31	0.02	0.03	0.00	0.07	0.02	0.31	0.00	0.02	0.02	0.08	0.02	0.00	0.00	0.00
Total	99.98	98.81	99.51	99.35	98.69	98.90	99.34	99.81	100.72	98.63	98.69	101.44	99.17	99.97	98.90	99.16	99.02	98.71	99.30
Si	1.68	1.74	1.73	1.78	1.66	1.76	1.80	1.67	1.59	1.68	1.66	1.85	1.78	1.86	1.62	1.78	1.69	1.66	1.82
Ti	0.11	0.11	0.07	0.08	0.12	0.08	0.08	0.12	0.11	0.11	0.12	0.06	0.05	0.06	0.15	0.07	0.09	0.10	0.06
Al	0.35	0.28	0.34	0.26	0.37	0.23	0.23	0.36	0.35	0.30	0.37	0.20	0.32	0.15	0.46	0.29	0.38	0.40	0.20
Fe^{3+}	0.09	0.04	0.09	0.06	0.17	0.14	0.04	0.10	0.08	0.16	0.17	0.02	0.05	0.05	0.06	0.05	0.10	0.08	0.07
Cr	0.01	0.02	0.01	0.00	0.00	0.00	0.00	0.00	0.21	0.00	0.00	0.01	0.01	0.00	0.00	0.00	0.00	0.03	0.00
Fe^{2+}	0.18	0.26	0.10	0.19	0.12	0.11	0.23	0.18	0.20	0.12	0.12	0.31	0.15	0.28	0.21	0.19	0.14	0.11	0.16
Mn	0.005	0.005	0.004	0.006	0.006	0.004	0.004	0.005	0.007	0.006	0.006	0.007	0.004	0.006	0.004	0.003	0.006	0.002	0.003
Mg	0.64	0.61	0.72	0.68	0.60	0.73	0.69	0.62	0.56	0.67	0.60	0.70	0.73	0.72	0.54	0.70	0.64	0.68	0.75
Ca	0.90	0.89	0.90	0.90	0.87	0.91	0.89	0.90	0.84	0.91	0.87	0.83	0.87	0.84	0.91	0.88	0.91	0.90	0.90
Na	0.04	0.04	0.03	0.04	0.08	0.04	0.04	0.05	0.04	0.04	0.08	0.03	0.04	0.04	0.05	0.04	0.04	0.04	0.03
K	0.00	0.00	0.00	0.00	0.01	0.00	0.00	0.00	0.00	0.00	0.01	0.00	0.00	0.00	0.00	0.00	0.00	0.00	0.00
Wollastonite	52.50	50.26	52.29	50.61	54.68	51.75	49.11	53.13	52.56	53.60	54.68	44.98	49.82	45.69	54.72	49.77	53.97	53.36	49.76
Enstatite	37.24	34.76	41.67	38.58	37.83	41.86	38.15	36.39	35.22	39.17	37.83	37.91	41.38	39.03	32.48	39.47	38.00	39.92	41.53
Ferrosilite	10.26	14.98	6.04	10.81	7.49	6.40	12.74	10.48	12.22	7.23	7.49	17.11	8.80	15.27	12.80	10.76	8.03	6.72	8.71
Mn/Fe^{2+}	0.03	0.02	0.03	0.03	0.05	0.03	0.02	0.03	0.04	0.05	0.05	0.02	0.02	0.02	0.02	0.02	0.04	0.02	0.02

Cations calculated based on 6 oxygens

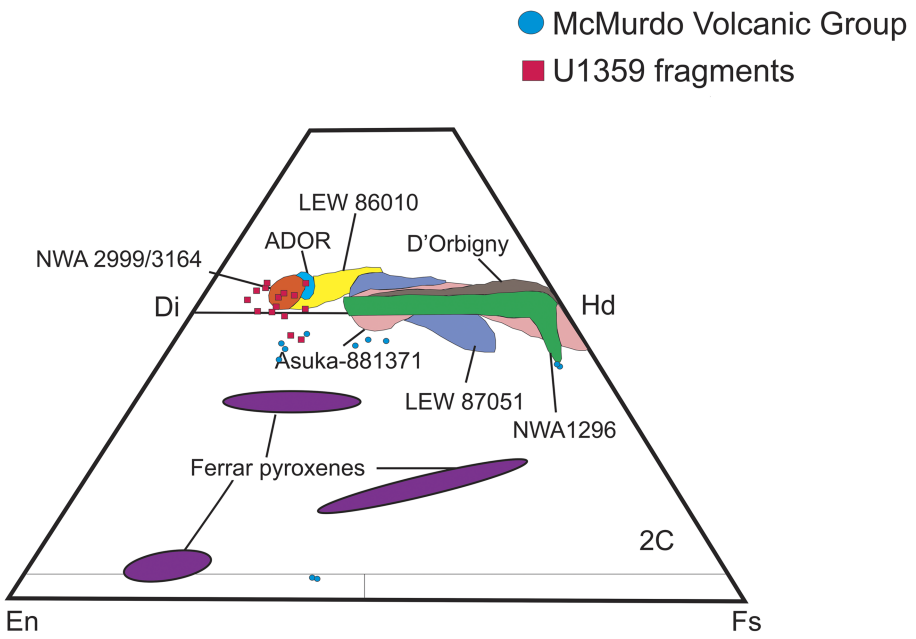

Fig. 5. Major element composition of clinopyroxene in basaltic fragments F2, F3 and F4 from Site U1359 plotted (red squares) in the pyroxene classification diagram (En: enstatite, Fs: ferrosilite, Di: diopside, Hd: hedenbergite). Al–Ti diopside–hedenbergite compositions from plutonic and volcanic angrites (Keil 2012) and terrestrial clinopyroxenes from Ferrar volcanic rocks (Elliot *et al.* 1995) are shown for comparison. High Ca-clinopyroxenes from the McMurdo Volcanic Group (blue circles, data from Nardini *et al.* 2003) are also shown.

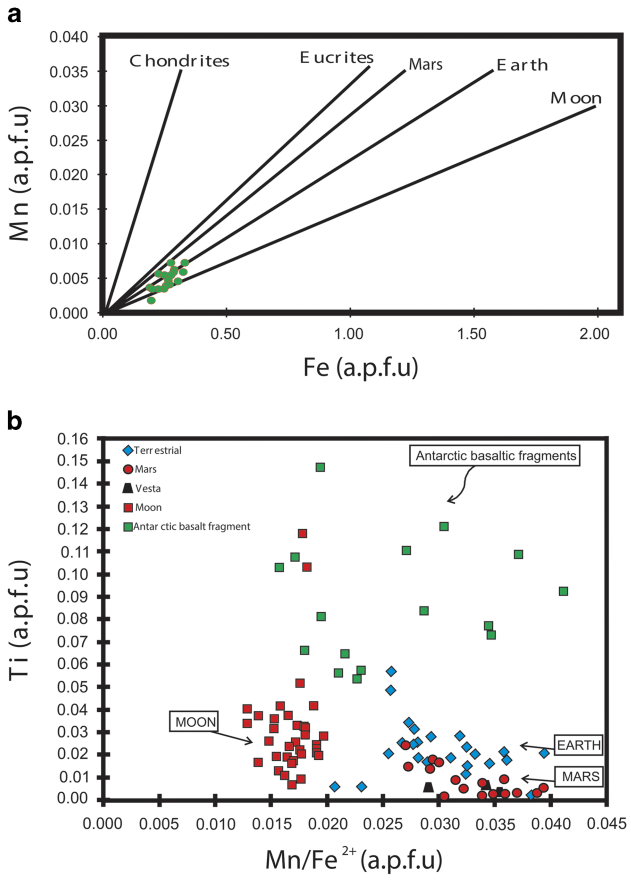

Fig. 6. Plots of **a.** Fe^{2+} *vs* Mn and **b.** Mn/Fe^{2+} *vs* Ti (in a.p.f.u.), for high Al–Ti diopside–hedenbergite from basaltic fragments F2, F3 and F4 from Site U1359. The regression lines in **a** for various clinopyroxene sources, as well as comparative data in **b**, are after Papike (1998).

not commonly reported, except for very rare grains of metamorphic or secondary high-temperature "deuteric" origin in calcareous and calc-silicate metamorphic rocks (e.g. Hirokazu 2005), or phenocryst and matrix clinopyroxene in alkaline basalts (e.g. Ngounouno *et al.* 2003). The basaltic fragments recovered from IODP Site U1359 have typical intergranular igneous textures (Fig. 4) and their clinopyroxenes do not exhibit secondary alteration features. Hence, the high Al–Ti diopside–hedenbergite pyroxenes in these rocks are of igneous origin. These minerals are also compositionally distinct from those in the local bedrock basalts of the Ferrar Large Igneous Province (Elliot *et al.* 1995). Pyroxenes from the Ferrar basalts cluster towards the enstatite and augite fields, whereas the Ca–Al–Ti pyroxenes of the U1359 basaltic fragments plot close to and above the diopside field (Fig. 5). Although uncommon in terrestrial basalts, Al–Ti diopside–hedenbergite pyroxenes have been widely reported in meteorites (e.g. Srinivasan *et al.* 2000). In summary, described basalts could represent part of metasomatized crust xenoliths linked with extensive magmatic rocks of Ferrar Large Igneous Province, in a process similar to that described in the India Ridge (Seyler *et al.* 2004), but in this case the clinopyroxene composition (rich in Ti and Al) is not described in any previous metasomatized mantelic basalts.

The Ti–Mn/Fe^{2+} and Mn versus Fe^{2+} plots of clinopyroxenes in U1359 basalt fragments can assist in distinguishing terrestrial and non-terrestrial pyroxenes (Fig. 6). Mn–Fe^{2+} compositions of some of the clinopyroxenes indicate similarities with pyroxene from

https://doi.org/10.1017/S0954102018000299 Published online by Cambridge University Press

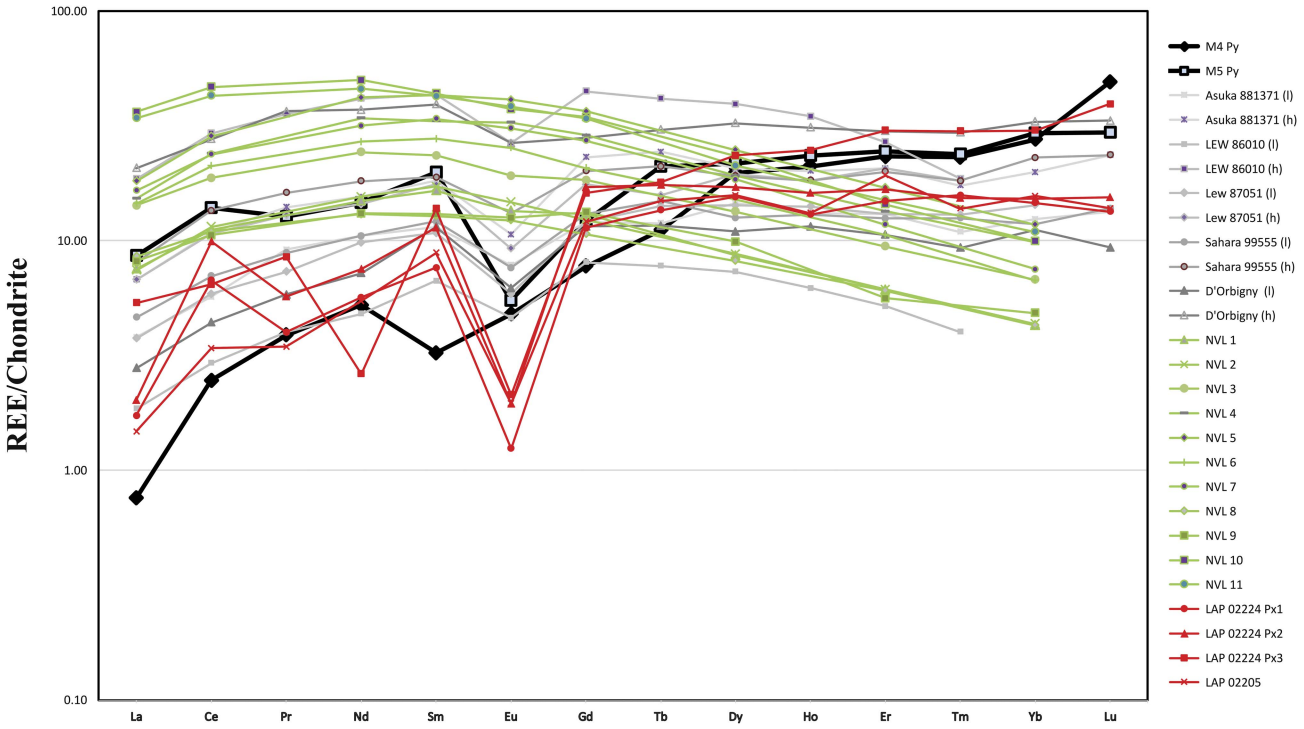

Fig. 7. Rare earth element concentrations in high Al–Ti diopside–hedenbergite from basaltic fragment F2 from Site U1359 (M4 Py and M5 Py) compared to clinopyroxene compositions in various angrites.

lunar rocks, although there is some overlap with terrestrial clinopyroxenes (Fig. 6a), and suggest a source more depleted in volatile elements compared to the Earth. The Ti–Mn/Fe^{2+} plot shows wide scatter but, significantly, none of the analysis plots within the field of terrestrial clinopyroxenes (Fig. 6b). Moreover, the REE patterns of clinopyroxenes in F2 closely match those of the angrite group of achondritic meteorites recovered from Antarctica and other locations (Fig. 7) (Floss *et al.* 2003, Keil 2012).

Opaque minerals in one basaltic fragment contain merrillite (Fig. 4b), a common phosphate mineral in meteorites (Xie *et al.* 2015), an anhydrous Ca-phosphate. The high fluorine content of analysed merrillite is likely to be incorporated as part of the PO_4 tetrahedra replacing oxygen (Gnos *et al.* 2002) or as part of solid solution with SiO_4 type of structures similar to that suggested by Moore (1983) for whitlockite related solid solutions. Occasionally, significant fluorine content (> 1weight %) is reported in merrillite which is generally a volatile free extraterrestrial phosphate such as from shergottite group gabbroic meteorites (Gnos *et al.* 2002). The Na content is also typical of merrillite composition (McCubben *et al.* 2014). This merrillite grain has Fe and Mg concentrations similar to lunar meteorites (LAP022xx Group 3 meteorite, Sun & McDonough 1989, Zeigler *et al.* 2005, Jolliff *et al.* 2006), whereas its Na content is closer to that of Martian meteorites (Jolliff *et al.* 2006). In the Shergotty meteorite, apatite and merrillite occur together, and compositional distinction between the two mainly consists of higher Fe, Mg and Na in merrillite (McCubben *et al.* 2014). Nevertheless, apatite and merrillite differ in terms of OH content (McCubben *et al.* 2014), as merrillite is nominally anhydrous and apatite has significant OH abundance up to equivalent 8600 ppm H_2O. The absence of apatite in the U1359 meteorite may indicate magmatic conditions characterized by relatively low hydrogen fugacity and high temperature. The analysed grain also contains high Fe and Na, as well as Mg, and thus apatite can be ruled out. Laser Raman spectra of merrillite provide interesting data. With a single strong peak at 963 cm^{-1} (± 1 cm^{-1}) and no peak at 967 cm^{-1}, merrillite can be confirmed, and the presence of whitlockite excluded. Nevertheless, typical laser Raman spectra of merrillite have double peaks (Fig. 9), but experimental and natural sample studies of Suizhou meteorite have shown that double peaks of merrillite transform to a single peak as a result of shock metamorphism (Xie *et al.* 2002). Xie *et al.* (2013), working on the same meteorite, reported the presence of chlorapatite as an original phase that transformed to merrillite with a single peak Raman spectrum. This may also explain the presence of fluorine in the merrillite grain studied here. A single peak in merrillite also has

https://doi.org/10.1017/S0954102018000299 Published online by Cambridge University Press

Table IV. Major element analyses of titaniferous magnetite, ilmenite and merrillite in basaltic fragment F3 (Sample VII) from IODP site U1359.

Phase	Magnetite	Ilmenite	Merrillite
Analysis no.	6/1	7/1	14/1
SiO_2 (wt%)	1.95	0.17	9.23
TiO_2	23.48	51.12	1.34
Al_2O_3	3.44	0.09	4.07
Cr_2O_3	0.26	0.00	0.01
BaO	0.00	0.13	0.00
FeO	63.93	40.97	3.37
MnO	0.56	0.54	0.00
MgO	2.86	4.38	0.94
NiO	0.00	0.12	0.00
CaO	0.49	0.38	44.17
Na_2O	0.67	0.03	1.51
K_2O	0.06	0.00	0.41
P_2O_5	0.11	0.02	32.88
F	0.21	0.00	4.40
Cl	0.01	0.00	0.18
Total	98.02	97.94	102.51
Si	0.07	0.00	3.43
Ti	0.67	0.97	0.38
Al	0.15	0.00	1.78
Cr	0.01	0.00	0.00
Fe^{2+}	2.03	0.86	1.05
Mn	0.02	0.01	0.00
Mg	0.16	0.16	0.52
Ca	0.02	0.01	17.61
Na	0.05	0.00	1.09
K	0.00	0.00	0.20
P	0.00	0.00	10.36
F	0.03	0.00	5.17
Cl	0.00	0.00	0.11

Cations calculated on 4 and 3 oxygen basis for magnetite and ilmenite, respectively

been described in lunar meteorites (Jolliff *et al.* 2006). Shock metamorphism could also have resulted in the formation of matrix glass with highly variable composition (Table II).

The absence of olivine in these rock fragments is difficult to explain, but plagioclase- and pyroxene-bearing ungrouped achondrites almost without olivine have been reported (e.g. NWA 011 and NWA2400) (Floss *et al.* 2005). The differentiated achondrites can also have low Ca plagioclases (Hutchison 2004). Considering their mineralogical and geochemical features, it is proposed that the basaltic fragments in Site U1359 sediments were sourced from achondritic meteorite. This source was probably similar to the angrite group with intergranular texture, mostly formed by Al–Ti–diopside–hedenbergite-rich pyroxene, olivine and calcic plagioclase (Mittlefehldt & Lindstrom 1990, Yanai 1994), and derived from one or more unidentified asteroidal sources (Greenwood *et al.* 2005). The plagioclase compositions of the identified basalt fragments are generally less calcic and richer in potassium than those in normal angrite (Table II), possibly due to subsolidus metasomatic changes through interaction with KREEP-like components. Similar compositions have been reported in lunar crustal rocks and have been ascribed to incompatible element enrichment during the evolution of the lunar magma ocean (Meyer & Hubbard 1970). However, although metasomatism is reported in angrites, its origin is currently unclear. The presence of potassium in plagioclase (Table II), and of anhydrous fluorine-rich Ca–Na phosphate merrillite (Fig. 4b, Table IV), supports that the parental magma of these fragments was similar to the enriched components in the lunar magma ocean. The sodium content of plagioclase is enigmatic.

O isotopic compositions in the clinopyroxene grain of the fragment F4 are consistent with differentiated meteorites (HED and angrites), and marginally overlap with those of ordinary chondrites (Table VI, Fig. 8). On the other hand, O isotopic compositions of the other three grains (2–4) of the fragment F4 are scattered along or plot slightly above the terrestrial fractionation line, and are not compatible with any meteorite (Table VI, Fig. 8). This trend may be an effect of local equilibration of O isotopes with seawater/ice in sediments, or an effect of snow on O isotopic composition (Misawa *et al.* 2010). It is possible a very small amount of (sea) water could have been introduced through the micro fracture in the fragment during a long period in the sediment under low temperature. Results are compatible with an extra-terrestrial origin affected by diagenesis or terrestrial fluids, but O isotopic results are inconclusive because of uncertainty.

Taken together, all the aforementioned compositional features support a non-terrestrial origin of the basalt fragments incorporated in the material drilled at Site U1359, and corroborate that marine sediments offshore of Terre Adélie were supplied with extra-terrestrial material during the Middle Pliocene to Plio-Pleistocene, or that reported basaltic fragments were eroded and transported in this margin during this period.

Ice-rafted origin of U1359 basalt fragments

It is highly probable that the basaltic fragments studied here and associated sediments were transported as IRD, given the overriding influence of the East Antarctic Ice Sheet on sedimentation in this region. Recent studies have demonstrated that the supply of most coarse sand grains to this continental rise site occurred by ice rafting (Patterson *et al.* 2014).

The lithologies of rock fragments and the petrology of heavy minerals in associated sediments are suggestive of a poly-metamorphosed bedrock source, constituted by low- to medium-grade metamorphic components generated at the amphibolite–granulite transition (Pant *et al.* 2013). Additional sediment-

https://doi.org/10.1017/S0954102018000299 Published online by Cambridge University Press

Table V. Trace element analyses of clinopyroxene in meteorite fragment F2 (M4 Py and M5 Py) and NIST 610 standard Pearce *et al.* 1997), compared to clinopyroxene compositions in different angrites.

	Fragment F2 (Sample IV)			Angrite clinopyroxene (Floss *et al.* 2003)										Mare basalt clinopyroxene (Anand *et al.* 2006, Day *et al.* 2006)				Basalts of Northern Victoria Land, Antarctica (Perinelli *et al.* 2011)										
Analysis no.	M4 Py	M5 Py	Average NIST 610	LEW 86010 (l)	LEW 86010 (h)	LEW 87051 (l)	LEW 87051 (h)	Sahara 99555 (l)	Sahara 99555 (h)	D'Orbigny (l)	D'Orbigny (h)	Asuka 881371 (l)	Asuka 881371 (h)	LAP 02224 Px1	LAP 02224 Px2	LAP 02224 Px3	LAP 02205	NVL 1	NVL 2	NVL 3	NVL 4	NVL 5	NVL 6	NVL 7	NVL 8	NVL 9	NVL 10	NVL 11
Sc (ppm)	355.90	358.08	444.28			133.00	29.00	187.00	87.00	219.00	11.00	204.00	71.00	115.00	138.00	51.30	118.00											
Co	1293.48	1176.13	408.20																									
Ni	1749.55	1151.32	445.55											536.00	602.00	358.00												
Rb	2.18	8.46	432.13											0.26	0.85	0.48	0.13											
Sr	2.87	8.43	498.12			19.00	35.00	17.00	32.00	12.00	70.00	23.00	30.00	6.03	8.23	4.37	6.00											
Y	28.81	37.48	449.40			21.00	31.00	21.00	31.00	19.00	64.00	20.00	31.00	20.70	25.00	39.70	21.30											
Zr	9.63	15.14	440.92			97.00	179.00	121.00	199.00	82.00	360.00	122.00	228.00	17.20	25.40	37.40	19.50											
Nb	<0.28	0.45	428.74																									
Ag	<0.50	<0.34	242.96																									
Ba	3.48	7.23	423.07			0.61	1.70	0.04	0.18	1.70	8.70	0.59	0.20	0.27	0.22	5.77	0.23											
La	0.18	2.04	467.37	0.44	4.40	0.89	1.60	1.10	1.90	0.66	4.90	0.90	1.60	0.41	0.48	1.27	0.35	1.79	1.76	3.37	3.62	4.31	3.44	3.92	2.02	1.93	8.63	8.11
Ce	1.51	8.53	447.72	1.80	18.00	3.60	6.60	4.30	8.30	2.70	17.00	3.50	6.70	4.11	6.07	3.96	2.09	6.83	7.05	11.5	14.7	17.5	12.96	14.6	6.72	6.49	28.7	26.3
Pr	0.36	1.18	428.78	0.37	3.30	0.68	1.20	0.82	1.50	0.54	3.40	0.85	1.30	0.37	0.53	0.79	0.32											
Nd	2.40	6.70	431.53	2.20	19.00	4.50	6.60	4.80	8.30	3.30	17.00	4.80	7.10	2.59	3.44	1.20	2.49	6.83	7.1	11.1	15.6	19.2	12.35	14.5	5.96	6.01	22.9	21
Sm	0.48	2.94	455.84	0.99	6.40	1.60	2.60	1.80	2.80	1.70	5.80	1.70	2.70	1.13	1.68	2.04	1.31	2.45	2.55	3.48	4.92	6.38	4.11	5.03	1.9	1.93	6.49	6.31
Eu	0.27	0.31	466.69	0.26	1.50	0.33	0.52	0.43	0.74	0.35	1.50	0.44	0.60	0.07	0.11	0.12	0.11	0.76	0.83	1.08	1.84	2.32	1.43	1.74	0.69	0.71	2.11	2.16
Gd	1.54	2.43	426.15	1.60	8.90	2.40	3.50	2.60	4.00	2.30	5.60	2.40	4.60	2.27	3.41	3.21	2.41	2.6	2.46	3.66	5.73	7.29	4.12	5.43	2.13	2.65	6.89	6.78
Tb	0.40	0.76	443.90	0.28	1.50	0.51	0.57	0.54	0.76	0.42	1.10	0.43	0.88	0.49	0.63	0.65	0.54											
Dy	4.86	5.33	431.56	1.80	9.70	3.50	4.80	3.10	4.70	2.70	8.00	3.60	5.10	3.82	4.21	5.78	3.88	2.12	2.15	3.3	4.72	6.1	3.72	4.55	2.01	2.44	5.76	5.23
Ho	1.15	1.28	450.99	0.34	1.90	0.77	1.00	0.71	1.00	0.63	1.70	0.72	1.10	0.71	0.88	1.35	0.72											
Er	3.72	3.92	426.12	0.83	4.30	2.10	3.30	2.00	3.20	1.70	4.80	2.10	3.30	2.38	2.67	4.83	3.08	0.98	0.98	1.51	2.15	2.72	1.7	1.88	0.97	0.9	2.3	2.41
Tm	0.57	0.59	425.92	0.10	0.46	0.32	0.45	0.31	0.45	0.23	0.73	0.27	0.43	0.39	0.38	0.74	0.34											
Yb	4.45	4.75	464.07			2.30		1.90	3.70	1.80	5.30	2.00	3.20	2.35	2.46	4.86	2.52	0.69	0.7	1.09	1.59	1.89	1.08	1.21	0.69	0.78	1.6	1.76
Lu	1.21	0.73	444.11					0.34	0.58	0.23	0.82	0.33	0.58	0.33	0.38	0.97	0.34											
Hf	0.75	1.33	417.94																									
Ta	1.23	4.91	378.57																									
W	0.62	4.29	454.41																									
Data source			Pearce *et al.* 1997																									

Table VI. Oxygen isotopic analyses of meteorite fragment F4 (Sample VIII) from IODP site U1359.

Analysis no.	1-a	1-b	1-c	2	3	4
Measured area	10 × 10 μm	8 × 8 μm	10 × 10 μm	8 × 8 μm	8 × 8 μm	8 × 8 μm
$\delta\,^{17}O_{SMOW}$ (‰)	1.1 ± 2.4	1.3 ± 2.4	2.4 ± 2.4	9.3 ± 2.4	5.9 ± 2.1	0.0 ± 2.7
$\delta\,^{18}O_{SMOW}$ (‰)	− 3.6 ± 1.5	2.3 ± 0.8	2.3 ± 1.1	10.8 ± 1.2	7.9 ± 1.4	2.9 ± 1.6

sourcing from the Ferrar Large Igneous Province, or another mafic igneous source of the Ross Orogen, is suggested by the Ordovician–Silurian age of monazite and xenotime grains dated using chemical geochronology (Pant *et al*. 2013). Additional sources for locally deposited IRD include the Transantarctic Mountains in Victoria Land, and Marie Byrd Land in West Antarctica (Fig. 1, sector d; Cook *et al*. 2013, Pant *et al*. 2013).

In the case that the obtained fragments were triggered by turbiditic currents along the Jussieu channel (Fig. 2), their source could have been even more proximal, and the fragments delivered from the near continental shelf. In any case, Early Palaeozoic bedrocks near the proximal Ninnis Glacier (Fig. 1, sector b) may have been a particularly important source for the studied site.

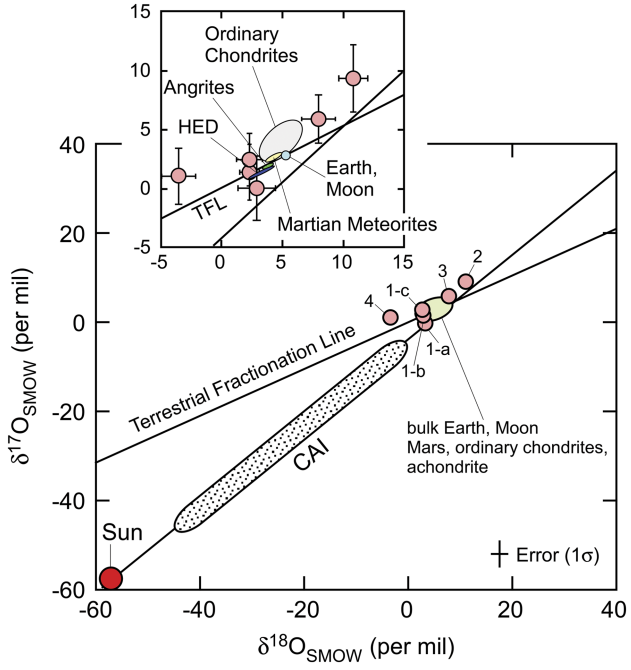

Fig. 8. Oxygen three-isotope plot of basaltic fragments analysed in this study (small circles) and representative compositions of major primary components of solar system materials (CAIs from carbonaceous chondrites, bulk Earth, Mars, ordinary chondrites, achondrites and the Sun) (Clayton 2003). HED stands for howardite–eucrite–diogenite meteorites. Representative1σ mean error bars are shown.

Conclusions

Four basaltic fragments, F1 to F4, have been analysed and identified as potential fragments of meteorites sourced from a rare achondrite differentiated meteorite. Major and trace element compositions of pyroxene grains (F2) and oxygen isotopes (F4) also point to a supply of extra-terrestrial material at IODP Site U1359. These basalt fragments have been recovered at various depths in marine sediments deposited between *c*. 2.7 and *c*. 1.01 Ma, suggesting they were supplied as IRD. Provenance studies on contemporaneous IRD suggest a range of potential West and East Antarctic sources, probably in the vicinity of the proximal Ninnis Glacier. Confirmation of the nature of the meteorite or unprecedented mantle paragenesis requires support from similar studies on the Plio-Pleistocene sediments in the vicinity of Site U1359.

Acknowledgements

This research used samples and data provided by the Integrated Ocean Drilling Program (IODP). The IODP is sponsored by the U.S. National Science Foundation (NSF), MEXT and participating countries under the management of Joint Oceanographic Institutions.

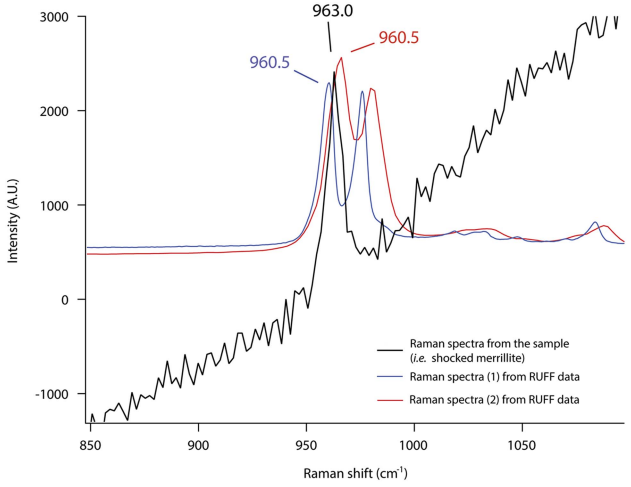

Fig. 9. Raman spectra of the sample from this study compared with spectra from the RRUFF database (http://rruff.info).

https://doi.org/10.1017/S0954102018000299 Published online by Cambridge University Press

The authors are indebted to Dr Atkins as editor, Dr Panter as reviewer, one anonymous reviewer, and Dr Akira Yamaguchi for their invaluable comments. NCP and PB acknowledge support from the National Centre for Antarctic and Ocean Research (NCAOR). We thank Nanophoton Corporation for providing Raman spectra analysis. Support for this study was provided to CE and FJE by the Spanish Ministry of Science and Innovation Grant CTM-2011-24079 and MEXT-Japan. RMK acknowledges funding from the Royal Society of New Zealand Rutherford Discovery Fellowship scheme (RDF-13-VUW-003). CM's research is supported by a Ramón y Cajal Fellowship (RYC-2012-11314). TvDF acknowledges funding from NERC (Grant NE/H014144/1) and the European Commission (Grant IRG 230828). MI acknowledges support by a JSPS Grant-in-Aid for Scientific Research (B), Grant Number 26287142, and by the JSPS Strategic Fund for Strengthening Leading Edge Research and Development to JAMSTEC.

Author contributions

NCP and FJJE designed the research; NCP, PB, DU and PKS performed the identification of the heavy mineral and meteorite fragments, FJJE was responsible for trace element analysis, and RM and CE carried out sedimentological description; CPC, NCP and TvDF performed the provenance and sources identification; MI, KS, JK, FJJE, YT, RS and KS performed platinum group, osmium isotopic and oxygen isotopic analysis; NCP, PB, DU and CM performed petrologic description. All authors contributed to the interpretation of the data. NCP, FJJE and CPC wrote the paper, with input from all authors.

References

Anand, M., Taylor, L.A., Floss, C., Neal, C.R., Terada, K. & Tanikawa, S. 2006. Petrology and geochemistry of LaPaz Icefield 02205: a new unique low-Ti mare-basalt meteorite. *Geochimica et Cosmochimica Acta*, **70**, 10.1016/j.gca.2005.08.018.

Clayton, R.N. 2003. Oxygen isotopes in meteorites. *In* Holland, H.D. & Turekian, K.K., *eds. Treatise on geochemistry*, Vol. 1. Amsterdam: Elsevier, 129–142.

Cook, C.P., van De Flierdt, T., Williams, T. *et al.* 2013. Dynamic behavior of the East Antarctic ice sheet during Pliocene warmth. *Nature Geoscience*, **6**, 10.1038/ngeo1889.

Day, J.M., Taylor, L.A., Floss, C., Patchen, A.D., Schnare, D.W. & Pearson, D.G. 2006. Comparative petrology, geochemistry, and petrogenesis of evolved, low-Ti lunar mare basalt meteorites from the LaPaz Icefield, Antarctica. *Geochimica et Cosmochimica Acta*, **70**, 10.1016/j.gca.2005.11.015.

Elliot, D.H., Fleming, T.H., Haban, M.A. & Siders, M.A. 1995. Petrology and mineralogy of the Kirkpatrick Basalt and Ferrar Dolerite, Mesa Range Region, North Victoria Land, Antarctica. *Antarctic Research Series*, **67**, 103–141.

Escutia, C., Brinkhuis, H., Klaus, A. & Expedition 318 Scientists. 2011. Wilkes Land glacial history: Expedition 318 of the riserless drilling platform Wellington, New Zealand, to Hobart, Australia Sites U1355–U1361, 3 January–8 March 2010. *Proceedings of the Integrated Ocean Drilling Program*, Vol. 318. Tokyo: Integrated Ocean Drilling Program Management International, Inc.

Floss, C., Taylor, L.A., Promprated, P. & Rumble III, D. 2005. Northwest Africa 011: a "eucritic" basalt from a non-eucritic parent body. *Meteoritics and Planetary Science*, **40**, 343–360.

Floss, C., Crozaz, G., McKay, G., Mikouchi, T. & Killgore, M. 2003. Petrogenesis of angrites. *Geochimica et Cosmochimica Acta*, **67**, 10.1016/S0016-7037(03)00310-7.

Fretwell, P., Pritchard, H., Vaughan, D. *et al.* 2013. Bedmap2: improved ice bed, surface and thickness datasets for Antarctica. *The Cryosphere*, **7**, 10.5194/tc-7-375-2013.

Gnos, E., Hofmann, B., Franchi, I.A., Al-Kathiri, A., Hauser, M. & Mauser, L. 2002. Sayh al Uhaymir 094: a new Martian meteorite from the Oman desert. *Meteoritics & Planetary Science*, **37**, 835–854.

Goodge, J. & Fanning, C. 2010. Composition and age of the East Antarctic Shield in eastern Wilkes Land determined by proxy from Oligocene–Pleistocene glaciomarine sediment and Beacon supergroup sandstones, Antarctica. *Geological Society of America Bulletin*, **122**, 10.1130/B30079.1.

Greenwood, R.C., Franchi, I.A., Jambon, A. & Buchanan, P.C. 2005. Widespread magma oceans on asteroidal bodies in the early Solar System. *Nature*, **435**, 10.1038/nature03612.

Hirokazu, T. 2005. Sadanagaite and fassaite from the contact aureole at the Kiura Kozan area, central Kyushu, Japan. *Proceedings of the Institute of Natural Sciences, Nihon University*, **40**, 107–112.

Hutchison, R. 2004. *Meteorites: a petrologic, chemical and isotope synthesis*. Cambridge: Cambridge University Press, 520 pp.

Ito, M. & Messenger, S. 2008. Isotopic imaging of refractory inclusions in meteorites with the NanoSIMS 50L. *Applied Surface Science*, **255**, 10.1016/j.apsusc.2008.05.095.

Jolliff, B.L., Hughes, J.M., Reeman, F.J.J. & Zeigler, R.A. 2006. Crystal chemistry of lunar merrillite and comparison to other meteoritic and planetary suites of whitlockite and merrillite. *American Mineralogist*, **91**, 10.2138/am.2006.2185.

Keil, K. 2012. Angrites, a small but diverse suite of ancient, silica-undersaturated volcanic-plutonic mafic meteorites, and the history of their parent asteroid. *Chemie der Erde-Geochemistry*, **72**, 10.1016/j.chemer.2012.06.002.

McCubben, M., Shearer, C.K., Burger, P.V., Hauri, E.H., Wang, J., Elardo, S.M. & Papike, J.J. 2014. Volatile abundances of coexisting merrillite and apatite in the Martian meteorite Shergotty: implications for merrillite in hydrous magmas. *American Mineralogist*, **99**, 10.2138/am.2014.4782.

Meyer, C. & Hubbard, N.J. 1970. High potassium and high phosphorous glass as an important rock type in the Apollo 12 soil samples. *Meteoritics*, **5**, 210–211.

Misawa, K., Kohno, M., Tomiyama, T., Noguchi, T., Nakamura, T., Nagao, K., Mikouchi, T. & Nishizumi, K. 2010. Two extraterrestrial dust horizons found in the Dome Fuji Ice core, East Antartica. *Earth and Planetary Science Letters*, **289**, 10.1016/j.epsl.2009.11.016.

Mittlefehldt, D.W. & Lindstrom, M.M. 1990. Geochemistry and genesis of the angrites. *Geochimica et Cosmochimica Acta*, **54**, 10.1016/0016-7037(90)90135-8.

Moore, P.B. 1983. Cerite, $Re_9(Fe^{3+},Mg)(Si0_4)_6(Si_40H)(OH)_3$: Its crystal structure and relation to whitlockite. *American Mineralogist*, **68**, 996–1003.

Nardini, I., Armienti, P., Rocchi, S. & Burgess, R. 2003. ^{40}Ar-^{39}Ar chronology and petrology of the Miocene rift-related volcanism of Daniell Peninsula (Northern Victoria Land, Antarctica). *Terra Antarctica*, **10**, 39–62.

Ngounouno, I., Déruelle, B., Demaiffe, D. & Montigny, R. 2003. Petrology of the Cenozoic volcanism in the Upper Benue valley,

northern Cameroon (Central Africa). *Contributions to Mineralogy and Petrology*, **145**, 10.1007/s00410-002-0438-6.

Pant, N.C., Biswas, P., Shrivastava, P.K., Bhattacharya, S., Verma, K., Pandey, M. & IODP Expedition 318 Scientific Party 2013. Provenance of Pleistocene sediments from site U1359 of the Wilkes Land IODP Expedition: evidence for multiple sourcing from east Antarctic craton and Ross orogeny. *Geological Society of London, Special Publications*, **381**, 277–297.

Papike, J.J. 1998. Comparative planetary mineralogy: chemistry of melt-derived pyroxene, feldspar, and olivine. *Reviews in Mineralogy and Geochemistry*, **36**, 7.1–7.11.

Patterson, M.O., McKay, R., Naish, T. *et al*. 2014. Orbital forcing of the East Antarctic ice sheet during the Pliocene and Early Pleistocene. *Nature Geoscience*, **7**, 10.1038/ngeo2273.

Pearce, N.J., Perkins, W.T., Westgate, J.A., Gorton, M.P., Jackson, S.E., Neal, C.R. & Chenery, S.P. 1997. A compilation of new and published major and trace element data for NIST SRM 610 and NIST SRM 612 glass reference materials. *Geostandards and Geoanalytical Research*, **21**, 10.1111/j.1751-908X.1997.tb00538.x.

Perinelli, C., Armienti, P. & Dallai, L. 2011. Thermal evolution of the lithosphere in a rift environment as inferred from the geochemistry of mantle cumulates, northern Victoria Land, Antarctica. *Journal of Petrology*, **52**, 665–690.

Seyler, M., Lorand, J.-P. & Gaston, G. 2004. Asthenospheric metasomatism beneath the mid-ocean ridge: evidence from depleted abyssal peridotites. *Geology*, **32**, 10.1130/G20191.1.

Srinivasan, G., Huss, G.R. & Wasserburg, G.J. 2000. A petrographic, chemical and isotopic study of calcium-aluminum-rich inclusions and aluminum-rich chondrules from the Axtell (CV3) chondrite. *Meteoritics and Planetary Science*, **35**, 10.1111/j.1945-5100.2000.tb01520.x.

Sun, S. & McDonough, W.F. 1989. Chemical and isotopic systematics of oceanic basalts: implications for mantle composition and processes. *Geological Society of London, Special Publications*, **42**, 313–345.

Tauxe, L., Stickley, C., Sugisaki, S. *et al*. 2012. Magneto and biostratigraphic constraints for the paleoceanographic record of the Wilkes Land Margin cores: IODP Expedition 318. *Paleoceanography*, **27**, 2214.

Xie, X., Yang, H., Gu, X. & Downs, R.T. 2015. Chemical composition and crystal structure of merrillite from the Suizhou meteorite. *American Mineralogist*, **100**, 2753–2756.

Xie, X., Zhai, S., Chen, M. & Yang, H. 2013. Tuite, γ-Ca3(PO4)2, formed by chlorapatite decomposition in a shock vein of the Suizhou L6 chondrite. *Meteoritics and Planetary Science*, **48**, 10.1111/maps.12143.

Xie, X., Minitti, M.E., Chen, M., Mao, H.K., Wang, D., Shu, J. & Fei, Y. 2002. Natural high-pressure polymorph of merrillite in the shock vein of the Suizhou meteorite. *Geochimica et Cosmoschimica Acta*, **66**, 10.1016/S0016-7037(02)00833-5.

Yanai, K. 1994. Angrite Asuka-881371: preliminary examination of a unique meteorite in the Japanese collection of Antarctic meteorites. *Proceedings of the NIPR Symposium on Antarctic Meteorites*, **7**, 30–41.

Zeigler, R.A., Korotev, R.L., Jolliff, B.L. & Haskin, L.A. 2005. Petrology and geochemistry of the La Paz Ice field basaltic lunar meteorite and source-crater pairing with Northwest Africa 032. *Meteoritics and Planetary Science*, **40**, 10.1111/j.1945-5100.2005.tb00174.x.